Supplementary Information

Enhanced Cyclability of Rechargeable Li-O_2 Batteries Enabled by Boron Carbide

Chaozhu Shu[a, b], Rui Huang[a], Jia Wang[a] and Dangsheng Su[a*]

[a] Shenyang National Laboratory for Materials Science, Institute of Metal Research, Chinese Academy of Science, Shenyang, PR China

[b] College of Materials and Chemistry & Chemical Engineering, Chengdu University of Technology, Chengdu, PR China

* Corresponding author. E-mail: dssu@imr.ac.cn, dangsheng@fhi-berlin.mpg.de.
Fax: (+86) 24-8397-0019

Experimental Section

Preparation of gas diffusion electrodes and cell assembly. The non-aqueous Li-O_2 cells were prepared using 2032-type coin cell. The O_2 catalytic electrodes were prepared by casting a mixture of 80% catalyst and 20% PVDF or 80% Super P and 20% PVDF onto a carbon paper disk (TGP-H-060). The mass loading of the B_4C catalyst (Aladdin Chemistry Co. Ltd.) was 0.3 mg cm^{-2}. The prepared cathode was heated at 100^{o}C for 12h under vacuum to remove solvent. The batteries were assembled in a glovebox filled with pure argon using a lithium foil as anode, a Whatman glass fiber separator and 1M LiTFSI (lithium bis-(trifluoromethanesulfonyl)-imide)) in TEGDME (tetraethylene glycol dimethyl ether) as electrolyte. After completing assembling, the batteries were transferred to a sealed

glass container filled with high-purity oxygen.

Materials characterization. XRD patterns were recorded on a Rigaku D/Max-2500PC diffractometer with Cu Ka radiation operation at 50kV and 300mA. Morphology structures were analysed using scanning electron microscopy (SEM, FEI Nova NanoSEM 450), and transmission electron microscope (TEM, FEI Tecnai G2 F20). Nitrogen adsorption-desorption data were measured with a Microneritics ASAP 2020 analyser at 77K. Piror to the measurements, the samples were degassed at 120^{o}C for 12h. The specific surface areas were calculated by the Brunauer-Emmett-Teller (BET) method using adsorption data. The pore size distributions (PSD) were calculated from adsorption data of isotherms using the Barrett-Joyner-Halenda (BJH) model. For discharged/charged cathode characterization, cell was disassembled in glovebox then cathode was washed thoroughly by acetonitrile and was dried for 20h under vacuum condition. NH_3 –TPD experiments were conducted in a conventional flow apparatus equipped with a thermal conductivity detector. The sample (50 mg) was pretreated under a helium stream flow (50mL min^{-1}) at 100 ^{o}C for 1h and then flushed with a mixture of NH_3 (5 vol%)-He for 1h at 100 ^{o}C. Subsequently, the sample was outgassed at the same temperature for 1h in helium stream to remove physisorbed ammonia. The TPD of NH_3 was measured from 50 to 650 ^{o}C at a heating rate of 10 ^{o}C min^{-1}.

Electrochemical measurements. The electrochemical performance of the Li-O_2 batteries was evaluated in 1 atm O_2 atmosphere using a LAND CT2001A battery testing system at room temperature. Before testing, the batteries were placed into a

close glass box which was flushed with pure O_2 for 6h. The specific capacity was calculated based on the amount of catalyst+PVDF in the cathode. The linear sweep voltammograms were recorded under O_2 atmosphere for B_4C based electrodes with a potential scanning rate of 0.1 mV s^{-1} at room temperature controlled by a VMP3 potentiostat/galvanostat. The electrochemical impedance spectroscopy (EIS) measurements were performed using a VMP3 potentiostat/galvanostat with EC-Lab® software (Bio-Logic Science Instruments). The DC voltage was maintained at open-circuit and an AC voltage was applied with an amplitude of 5 mV at a frequency range of 300 kHz to 50 mHz.

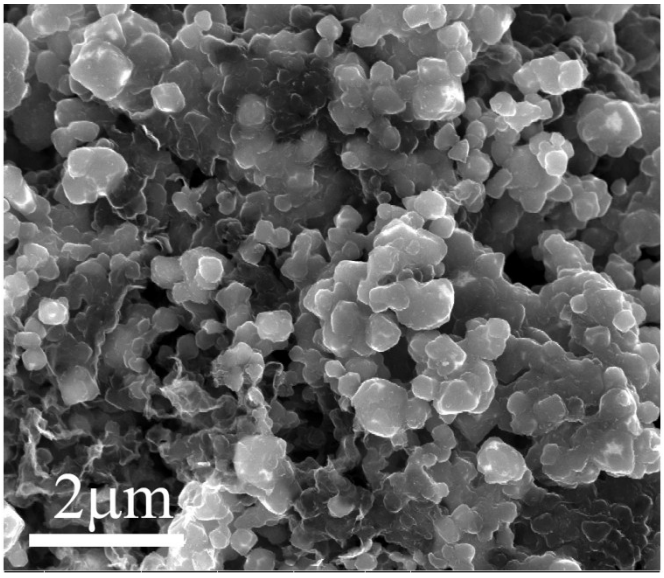

Figure S1. SEM image of the B_4C nanoparticles.

Clarifying the influence of the carbon paper on the battery.

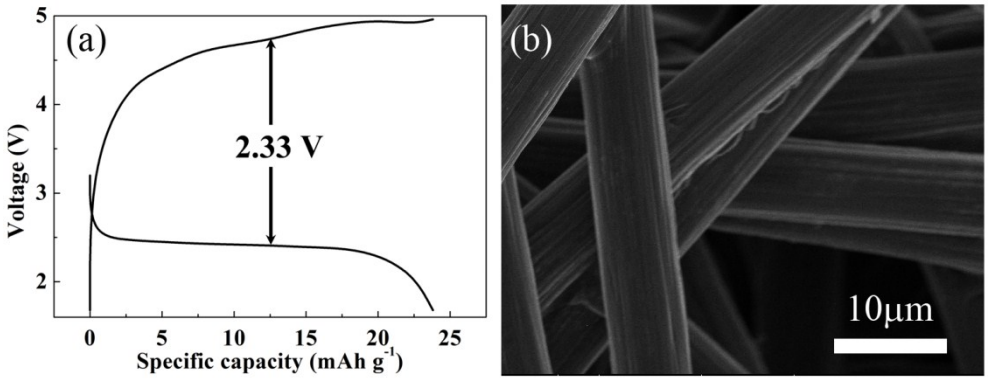

Figure S2: (a) discharge-charge curves of a blank Li-O_2 battery using only Toray carbon paper electrode at current density of 500 mA g^{-1} $_{B4C}$ (the same current as B_4C based electrode). (b) the morphology of carbon paper based electrode at the end of discharge.

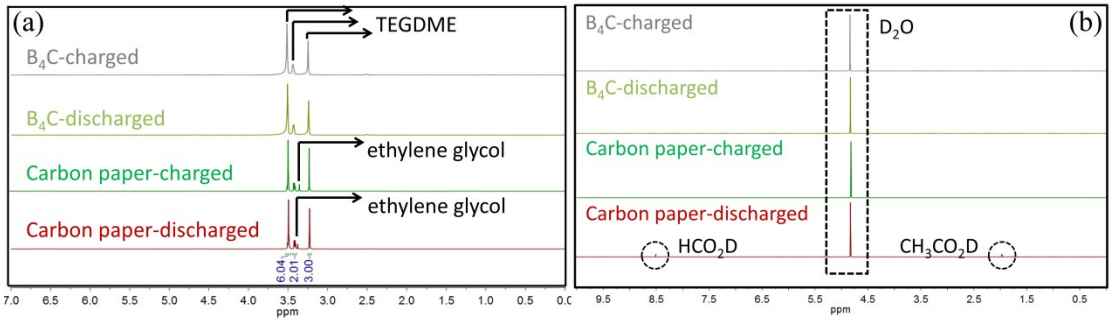

Figure S3: (a) ^{1}H NMR spectra of the TEGDME electrolyte of Li-O_2 cells with

carbon paper and B_4C based electrodes at the end of discharge and charge; (b) ^1H NMR spectra of carbon paper and B_4C electrodes extracted with D_2O at the end of discharge and charge.

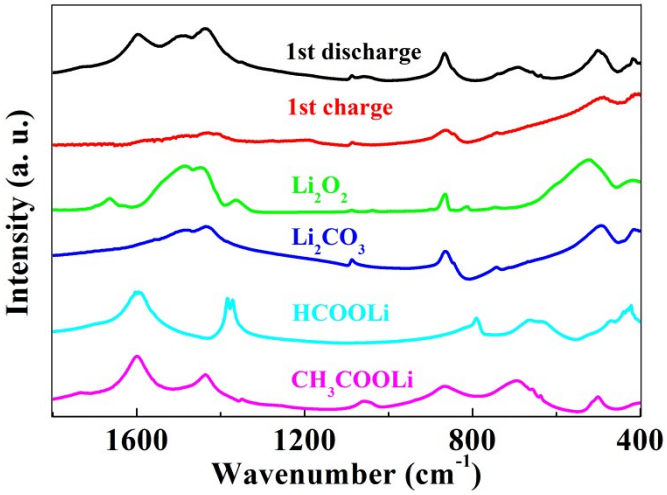

Figure S4: FTIR spectra of carbon paper based electrode at the end of discharge and charge. The reference spectra for Li_2O_2 (impurity peaks at 1080, 1450 and 1620 cm^{-1} are assigned to Li_2CO_3), Li_2CO_3, HCOOLi and CH_3COOLi are also shown.

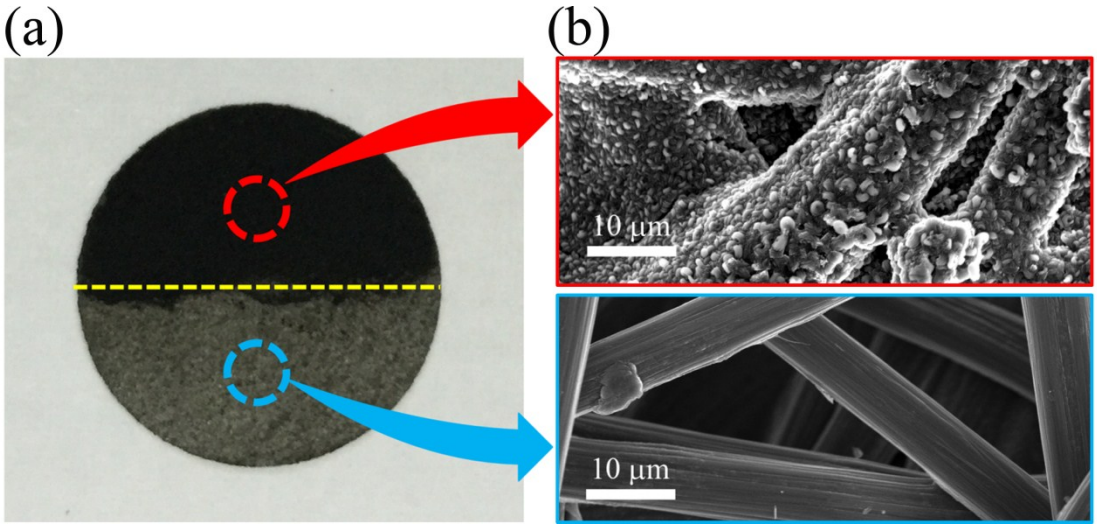

Figure S5: (a) specially designed electrode and (b) the morphology at the end of discharge.

As shown in Figure S2 (a), Li-O_2 battery with carbon paper electrode has been studied. It can be seen that the overpotential is higher for carbon paper based electrode (2.33 V) than that for B_4C based electrode (1.11 V, see Figure 2a in revised manuscript), and the capacity of carbon paper based Li-O_2 battery can almost be

neglected (< 25 mAh g^{-1}). There is nearly no product generated on carbon paper based electrode after discharging (figure S2 (b)). The significantly large overpotential and low specific capacity for carbon paper based Li-O_2 battery is caused by the following two possible reasons: (1) the sluggish kinetic rate caused by the poor activity of carbon paper for oxygen reduction reaction (ORR) and oxygen evolution reaction (OER); (2) the less space for product accommodation induced by the low BET surface area of carbon paper (surface area of carbon paper is so low that we cannot measure the value by nitrogen adsorption-desorption measurement). The large overpotential of carbon paper based Li-O_2 battery can result in the decomposition of cell components including electrolyte and electrode. After loading B_4C on carbon paper to form B_4C based electrode, the overpotential of Li-O_2 battery is significantly reduced, indicating that the improved catalytic activity of B_4C for oxygen electrode reaction. In addition, the electrochemical decomposition of electrolyte and carbon paper can also be circumvented due to the low overpotential of Li-O_2 battery based on B_4C cathode. To further unveil the origin of improved stability of B_4C based electrode, electrolyte and electrode stability after cycling were examined with ^1H nuclear magnetic resonance (NMR). The residual electrolyte in separator was extracted and then subjected to NMR spectroscopy with DMSO as solvent to reveal any decomposition product of electrolyte during Li-O_2 cell cycling. ^1H NMR results in Figure S3 (a) showed peaks assigned to TEGDME only and no other peaks were detected for B_4C based electrode. However, in the case of carbon paper based electrode, the peaks indicative of undesirable reaction were observed. The peaks around ~3.5 ppm in Figure S3 (a) demonstrated the presence of ethylene glycol. ^1H NMR spectra of carbon paper and B_4C electrodes extracted with D_2O after cycling was also shown in Figure S3 (b). Peak assignments reveal the presence of lithium formate and lithium acetate on carbon paper based electrode after discharging. The lack of any detectable lithium formate and lithium acetate evolution on B_4C based electrode confirms that the amount of electrolyte and electrode decomposition occurring on the B_4C based electrode are very smaller than that on carbon paper based electrode, demonstrating the improved stability of Li-O_2 battery with B_4C based electrode. The FTIR spectrum

on carbon paper electrode (Figure S4) shows that the discharge products contain lithium carbonate and organic carboxylate products, the peak of Li_2O_2 may be overlapped by that of Li_2CO_3. After charging, residues of Li_2CO_3 on carbon paper electrode were observed. For B_4C based electrode (B_4C loaded on carbon paper), electrochemical reaction mainly conducted on B_4C surface during ORR and OER due to the higher catalytic activity and larger surface area of B_4C compared to that of carbon paper. In other words, the formation and decomposition of Li_2O_2 mainly occurred on B_4C rather than on carbon paper. SEM result of our specially designed electrode (carbon paper was half-covered by B_4C, as shown in Figure S5 (a)) after discharging indicated that the toroid-like Li_2O_2 can only be found on B_4C (Figure S5 (b)), further confirming the mainly electrochemical reaction occurred on B_4C. Furthermore, there is no byproduct formed on carbon paper part of our specially designed electrode, confirming the inhibition of electrochemical corrosion of carbon paper by reduction of overpotential.

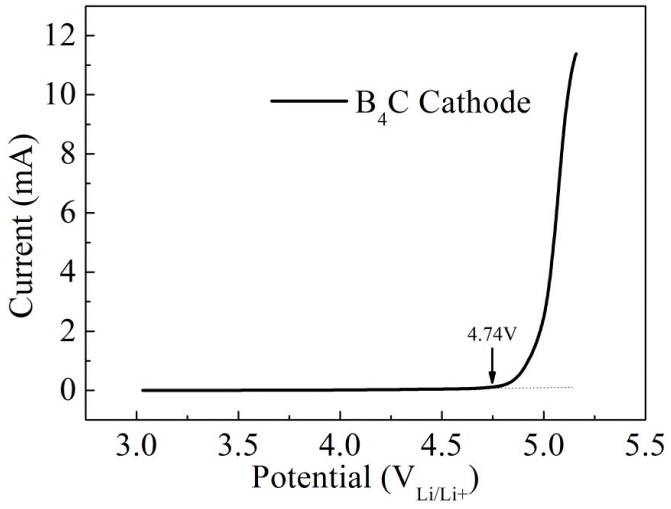

Figure S6. Anode stability of 1M LiTFSI/TEGDME electrolyte at 0.1 mV s^{-1} in O_2 atmosphere (1 atm). It can be clearly seen from the linear sweep scan voltammetry in the LiTFSI/TEGDME electrolyte that at a potential around 4.74 V (vs. Li/Li^+) the current diverges and becomes unstable, an indication that the electrolyte undergoes

massive decomposition at around this potential.

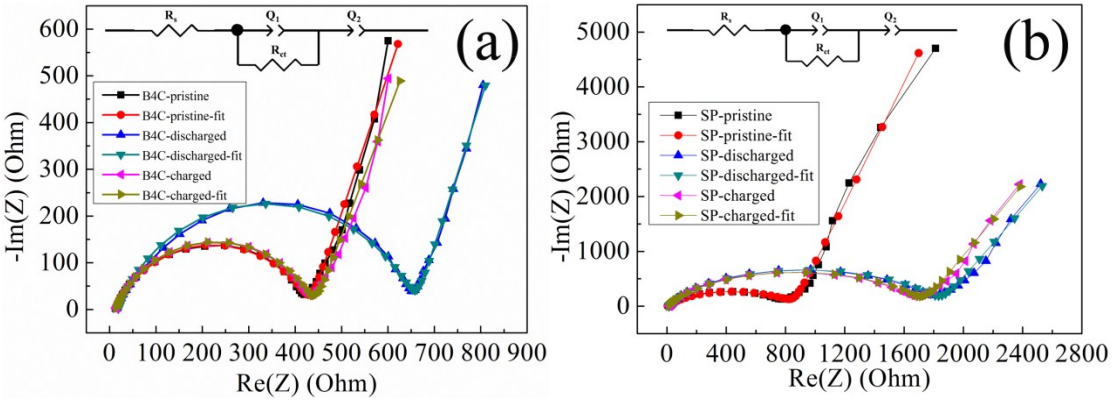

Figure S7. Nyquist plots of (a) B_4C based and (b) Super P based Li-O_2 battery. The inset shows the equivalent circuit.

Table S1. Parameters for Figure 3b, fitted by the equivalent circuit shown in the inset.

Element	**B_4C-Pristine**	**B_4C-Discharged**	**B_4C-Recharged**
Rs	11.9 Ohm	18.2 Ohm	12.2 Ohm
Q1	8.27 μF	6.48 μF	7.17 μF
***a*1**	0.738	0.781	0.752
Rct	420.4 Ohm	641.2 Ohm	429.5 Ohm
Q2	4.199 mF	5.072 mF	4.677 mF
***a*2**	0.7949	0.8056	0.7703

Table S2. Parameters for Figure S3, fitted by the equivalent circuit shown in the inset.

Element	**Super P-Pristine**	**Super P-Discharged**	**Super P-Recharged**
Rs	2.9 Ohm	12.5 Ohm	12.7 Ohm
Q1	8.75 μF	3.70 μF	3.73 μF

***a*1**	0.693	0.791	0.791
Rct	859.8 Ohm	1831 Ohm	1715 Ohm
Q2	0.5954 mF	1.109 mF	1.129 mF
***a*2**	0.8857	0.8054	0.8129

The equivalent circuit displayed above in Figure 3b and Figure S3 consists of an uncompensated ohmic resistance (Rs) in series with a constant phase element (Q1) in parallel with the charge transfer resistance (Rct). At the end of the circuit is a second constant phase element (Q2).The elements of Rs, Q1 and Rct cause the depressed semi-circle shape in the Nyquist plots, while the element Q2 is related to diffusion of active species to the surface of the electrode and gives rise to the linear tail following the semi-circle at low frequencies. The uncompensated resistance Rs is due to the electronic resistances of the electrodes, contacts, and electrolyte resistance and is roughly the same for each cell. The constant phase elements defines as Q and *a* represent the capacitive contributions of the each electrode, where the value of *a* can range between 0 and 1, with 0 being a pure resistor and 1 being a pure capacitor.

The polarization resistance (Rct) shows an increase of 53% and 113% after discharge of the cells with B_4C based and Super P based cathode, respectively, relative to the pristine cell. The degree of capacitance (Q2) resulting in the linear slop of the Nyquist plot at low frequencies is nearly the same for the discharged cell as for the pristine cell. This is because the formed Li_2O_2 film of the discharged cell does not significantly change the surface area or morphology of the underlying cathode. It is

likely that the polarization is caused by limited mass transport of Li^+ and/or O_2 to the active surface sites by the build-up of Li_2O_2 product rather than pore-blocking for the B_4C based cathode, since open pores are evident in the SEM images. Electrochemical impedance spectroscopy measurements reveal the increase in Rct after discharge and recovery after recharge for B_4C based Li-O_2 battery. However, the Rct of recharged cell obviously larger than the pristine cell for Super P based Li-O_2 battery. These results demonstrate that the discharged products on Super P electrode may not be decomposed completely after recharge.

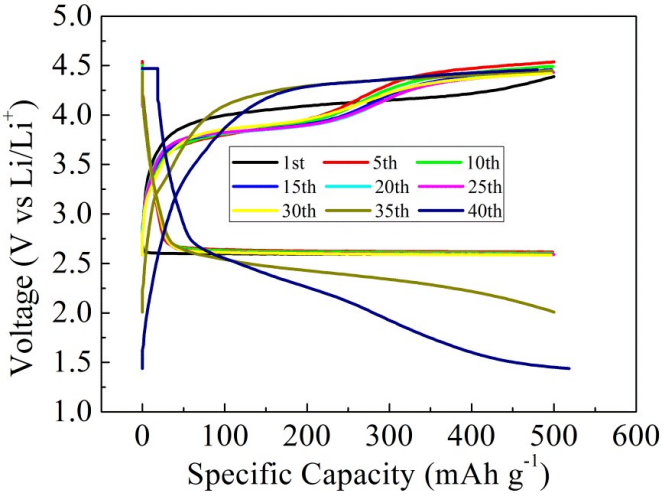

Figure S8. Cycling performance of Li-O_2 battery based on Super P cathode at 500 mA g^{-1} (0.15 mA cm^{-2}) by curtailing capacity to 500 mAh g^{-1} (0.15 mAh cm^{-2}).

Table S3. Recent results of carbon-free cathodes for Li-O_2 battery.

Cathode materials	Loading (mg cm^{-2})	(Dis)charge current density (mA g^{-1})	Cut-off capacity (mAh g^{-1})	Cycle number	Overpotential at the last cycle (V)[a]	References
TiC	4	250	350	100	~1.75	[S1]
Ru/ITO	6	25	~300	50	~1.75	[S2]
Ru/$TiSi_2$	0.1	100	1000	100	~1.4	[S3]
Au/Ni	0.081	~500	600	110	~2	[S4]

Pt/Co_3O_4	~0.5	100	500	55	~1.5	[S5]
2D-RuO_2	0.8	200	<1000	50	~1.7	[S6]
RuO_2 Hollow Sphere	0.3-0.5	500	~1000	100	~1.7	[S7]
Ru Nanosphere	0.8	500	1000	80	~1.25	[S8]
Ti_4O_7	1	500	~100	40	~1.25	[S9]
AgPd-Pd composite	2	200	1000	100	~1.4	[S10]
B_4C	0.3	1000	1000	>160	~1.8	This work

[a] Due to the overpotential gradually increasing during cycling, the overpotential of the last cycle is compared.

It can be clearly seen that the B_4C based electrode can be discharged and charged for over 160 cycles at cut-off capacity of 1000 mAh g^{-1} and higher current density of 1000 mA g^{-1} compared to literature results. The overpotential of the last cycle was compared due to the overpotential gradually increasing during cycling. It can be seen that the overpotential of the B_4C based electrode is slightly higher than other electrodes (1.8 V for B_4C compared to 1.7 V for RuO_2, 1.4 V for AgPd-Pd composite and 1.25 V for Ti_4O_7). This may be caused by the inferior conductivity of B_4C based electrode compared to those metal or metal oxide based electrodes. Notably, the higher (dis)charge current density and longer cyclability are also the reasons why B_4C based electrode has a slightly higher overpotentail at the last cycle.

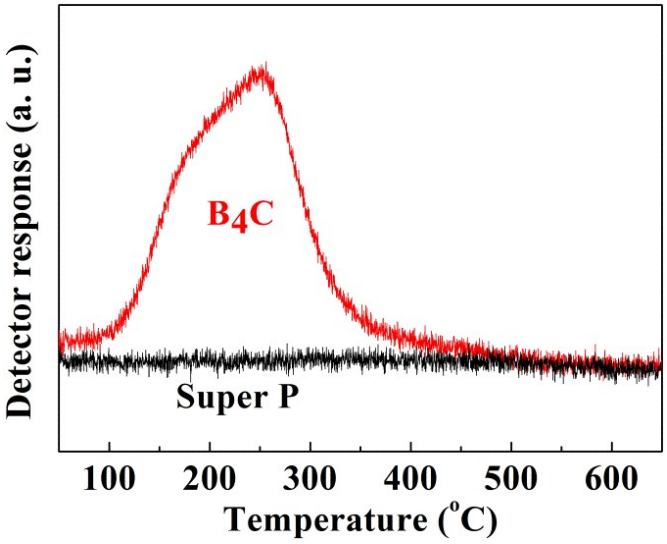

Figure S9. NH_3-TPD profiles of B_4C and Super P. The TPD profiles show that the

acid strength of B_4C was higher than that of Super P, which was indicated by a obvious desorption peak of NH_3.

Supplementary References

[S1] M. M. Ottakam Thotiyl, S. A. Freunberger, Z. Peng, Y. Chen, Z. Liu, P. G. Bruce, *Nat. Mater.*, 2013, **12**, 1050.

[S2] F. Li, D. M. Tang, Y. Chen, D. Golberg, H. Kitaura, T. Zhang, A. Yamada, H. Zhou, *Nano Lett.,* 2013, **13**, 4702.

[S3] J. Xie, X. Yao, I. P. Madden, D. E. Jiang, L. Y. Chou, C. K. Tsung, D. Wang, *J. Am. Chem. Soc.,* 2014, **136**, 8903.

[S4] S. T. Kim, N. S. Choi, S. Park, J. Cho, *Adv. Energy Mater.,* 2014, 1401030.

[S5] J. Cao, S. Liu, J. Xie, S. Zhang, G. Cao, X. Zhao, *ACS Catal.,* 2015, **5**, 241

[S6] K. Liao, X. Wang, Y. Sun, D. Tang, M. Han, P. He, X. Jiang, T. Zhang, H. Zhou, *Energy Environ. Sci.,* 2015,**8**, 1992

[S7] F. Li, D. M. Tang, T. Zhang, K. Liao, P. He, D. Golberg. A. Yamada, H. Zhou, *Adv. Energy Mater.,* 2015, **5**, 1500294

[S8] D. W. Su, S. X. Dou, G. X. Wang, *J. Mater. Chem. A,* 2015,**3**, 18384

[S9] D. Kundu, R. Black, E. J. Berg, L. F. Nazar, *Energy Environ. Sci.,* 2015,**8**, 1292

[S10] W. B. Luo, X. W. Gao, S. L. Chou, J. Z. Wang, H. K. Liu, *Adv. Mater.,* 24 September 2015 online. DOI: 10.1002/adma.201502262